Residual Stress and Texture Control in Ti-6Al-4V Wire + Arc Additively Manufactured Intersections by Stress Relief and Rolling

J. R. Hönnige[1], P. A. Colegrove[1], B. Ahmed[2], M. E. Fitzpatrick[2], S. Ganguly[1], T.L. Lee[3], S. W. Williams[1]

[1]Welding Engineering and Laser Processing Centre, Cranfield University, MK43 0AL Cranfield, UK

[2]Centre for Manufacturing and Materials Engineering, Coventry University, Priory Street, Coventry CV1 5FB, U.K.

[3]ISIS Facility, Rutherford Appleton Laboratory, Didcot, Oxfordshire OX11 0QX, UK

Abstract. Additively manufactured intersections have the theoretical risk to contain hydrostatic tensile residual stresses, which cannot be stress relieved. The stresses in Ti-6Al-4V Wire + Arc Additively Manufactured (WAAM) intersections are lower compared to single pass walls and stresses in continuous walls are larger compared to discontinuous wall with otherwise identical geometry. Thermal stress relief was found to virtually eliminate them.

Inter-pass rolling can yield the desired grain refinement, without having any noteworthy influence on the development of residual stresses. The strain measurement itself by neutron diffraction is facilitated by the refined microstructure, because the textured microstructure produces anisotropic peak intensity, not allowing Pawley refinement. The {1011} and {1013} hcp planes are the only ones that diffract consistently in three orthogonal directions.

1 Introduction

Process residual stresses are one of the main challenges in additive manufacturing (AM). Consequences can include severe distortion or premature failure of the component, during manufacture or in service. Wire + Arc Additive Manufacturing (WAAM), as a high-deposition-rate metal AM process, can be used for the manufacture of large meter-scale of medium complexity. It is especially appealing to the aero-space industry for producing structural components [1]. The alloy Ti-6Al-4V is probably the material to benefit most from the advantages of WAAM, due to commonly high material and processing costs and it is therefore the subject of this research. However, WAAM is especially prone to develop very large stresses, which is due to constrained cooling of each deposition, which prevents thermal contraction. The development is described elsewhere [2]–[5] and depending on the material, the residual stress can range from 60% to almost 100% of the materials' yield value. Tensile residual stresses (σ_{res}) are constant along the wall height and are typically the largest in longitudinal direction (σ_{xx}), as shown in Figure 1 (a).
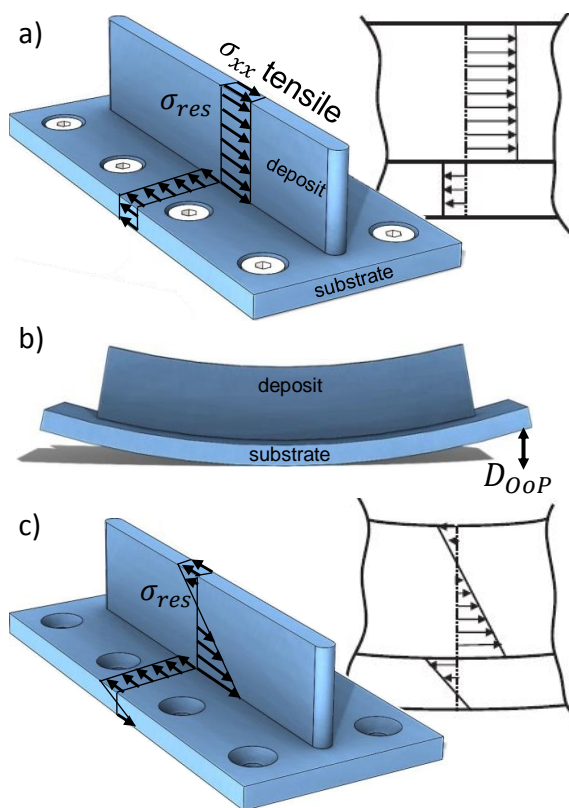

Figure 1: Typical residual stress profiles in WAAM and consequent distortion: (a) clamped residual stress profile; (b) out-of-plane distortion after unclamping and (c) redistributed and balanced residual stress profile after unclamping (adpt. from [4]).

Each layer adds additional material that develops the same tensile stress during constrained thermal shrinkage. These tensile stresses result in a bending moment across the cross-section. After unclamping, this causes the component to distort and the residual stresses σ_{res} to redistribute, as shown in Figure 1 (b) and (c). The resulting out-of-plane distortion (D_{OoP}) of a 400 mm-long Ti-6Al-4V wall for example can be as high as 7 mm [6].

Several residual stress mitigation techniques exist [7], of which only a few come into consideration due to process constraints. Thermal techniques involve for example stress relief at elevated temperatures [8]. The temperature range of heat treatments for microstructural improvements [9], [10] or even hot-isostatic pressing [11], [12] typically exceed stress relieving temperatures and act therefore stress relieving by default. Mechanical techniques can be vibratory stress relief [13] and acoustic softening [14]. High-pressure rolling is a local mechanical tensioning technique, which is used to plastically strain a weld seam or an additive deposit to counteract the stresses. It has shown to be very effective for eliminating residual stress and distortion in butt-welds [15]–[18]. In additive manufacturing, when applied in an inter-pass manner, its effect is more limited, as the stress and distortion in straight titanium walls can only be reduced, but not eliminated entirely. The reason is the absence of lateral restraint, resulting in lateral deformation rather than longitudinal straining, which would eliminate the residual stresses [2]–[4]. Attempts to constrain the transverse deformation during rolling significantly improve the distortion and residual stress reduction [4], [6]. Even though lateral constraining can eliminate distortion, significant and unevenly distributed residual stresses can persist. Furthermore local restraining becomes inpractical at varying wall widths or intersections. Therefore it seems that only post-deposition thermal stress relieving of the final component can be utilized for reliable stress elimination in additively manufactured structures [8] and especially intersections. Even though inter-pass rolling has limited capability to control residual stresses in Ti-6Al-4V WAAM, it significantly improves the microstructure. When rolling is applied after each layer, it can eliminate texture [19], decreases prior-β grain and α-lath size [20] and thereby improves mechanical properties [21]. This is currently the main motivation for inter-pass rolling [22].
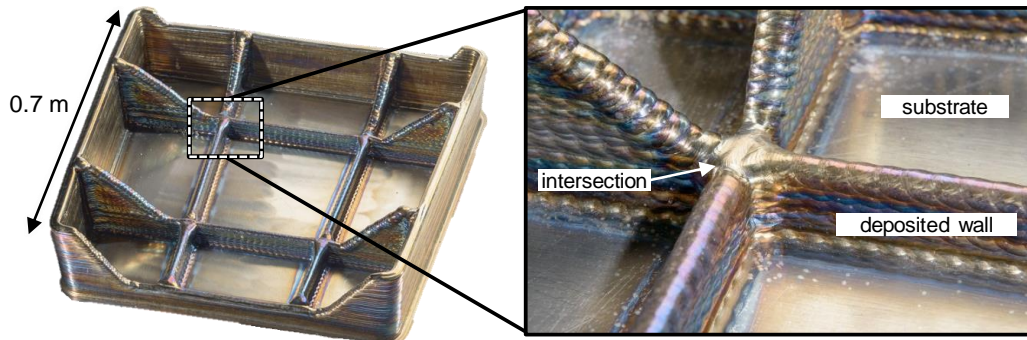
Figure 2: Typical WAAM application with intersections: Bombardier near-net-shape Ti-6Al-4V landing gear rib [6].

The manufacture of structural application components requires more complex features than straight and free-standing walls, such as curves and intersections, as shown in a typical WAAM application in Figure 2. This near-net-shape part of a 21 kg Bombardier landing gear rib is 0.7 x 0.7 x 0.3 m in dimension and weighs 24 kg in the as-deposited condition. To the authors' knowledge, no residual stress measurements have been performed on additively manufactured intersections. Only Mehnen *et al.* [23] simulated the stress in WAAM intersections of steel, which seemed to be less in the intersection compared to the free-standing walls. However, as the paper mainly discusses the strategy of producing different features, the stress development was not investigated in great detail, hence a comparison is not possible. The constraint in the transverse direction and the discontinuous deposition of the intersected region could significantly influence residual stress development. Also the application of inter-pass rolling can influence the residual stress development. A different behaviour may be observed when applied on intersections, as the lateral restraint might have a beneficial effect on the stress reduction as well. The established neutron diffraction stress measurement technique was performed to calculate the stress profiles in the three principal directions of the intersection, after which the destructive contour method was used for a more detailed insight into the stress distribution within the entire component. The contour method is based on stress relaxation and involves cutting through the section of interest by electro-discharge machining (EDM), after which the topography of the exposed surface contains the information of the relaxed stresses. The measured surface is post-processed using a 3D finite element model, by calculating the required stress to return the displaced surface back to a flat plane [24].

2 Materials and Experiments

Production of Specimen

Four Ti-6Al-4V intersecting walls were built with the deposition parameters from Table 1 using the in-house-built HiVE machine (High-Value Engineering). The HiVE (Figure 3) is a converted friction stir welding CNC gantry with a WAAM deposition unit retrofitted to the machine. The machine tool has been replaced by a customized roller device, which is capable of two-directional rolling with vertical rolling loads up to 100 kN. The deposition unit is attached to a rotator, allowing the coaxial rotation of the shield, wire feeder and wire spool around the plasma torch. A Fronius Plasma 10 module was used [25] to deposit 1.2-mm-diameter Ti-6Al-4V wire on a 12-mm-thick Ti-6Al-4V substrate that was clamped during the deposition to a rigid steel backing block, which prevented distortion during the deposition. For the first three layers the current was increased by 10% to compensate for the heat sinking effect of the substrate. A laminar flow local trailing shield [26] attached to the torch was used to prevent the deposited material from oxidising [27]. The plasma gas was pure-shield argon, as was the plasma shielding gas and the trailing shielding gas.
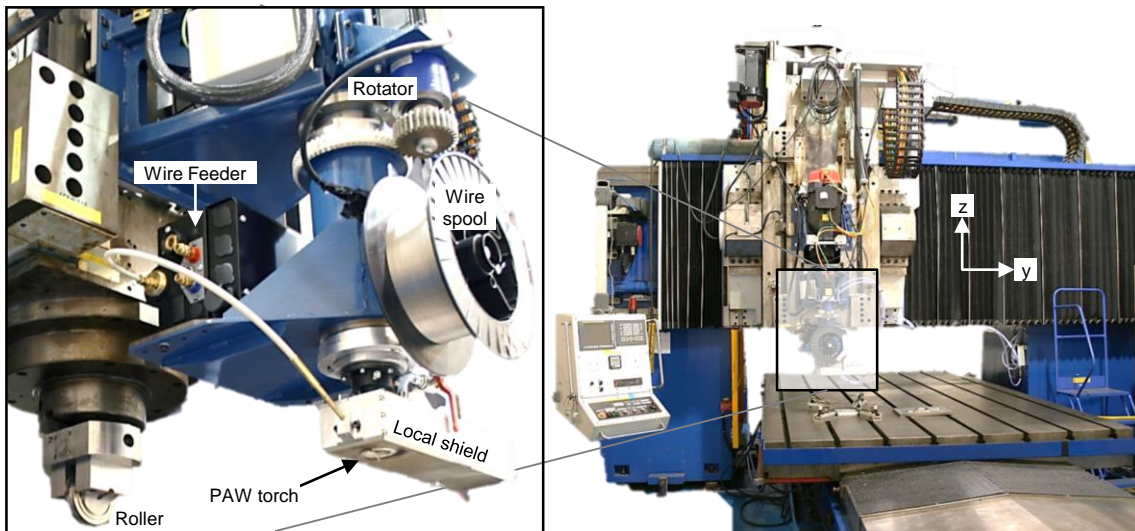

Figure 3: The "HiVE" build platform: WAAM deposition unit retrofitted with a rotator to the z-axis of a FSW machine; the FSW tool is replaced by a customised roller unit.

The oscillating path strategy, which is shown in the schematic in Figure 4, was used to produce the intersections: for odd layers (a), a continuous wall (I) was deposited in the x-direction with 6 mm oscillating width and a 3 mm step size. Two shorter lateral walls (II) & (III) with identical parameters to the first wall were deposited from the outside towards the centre in positive and negative y-direction respectively, until they joined the continuous wall.
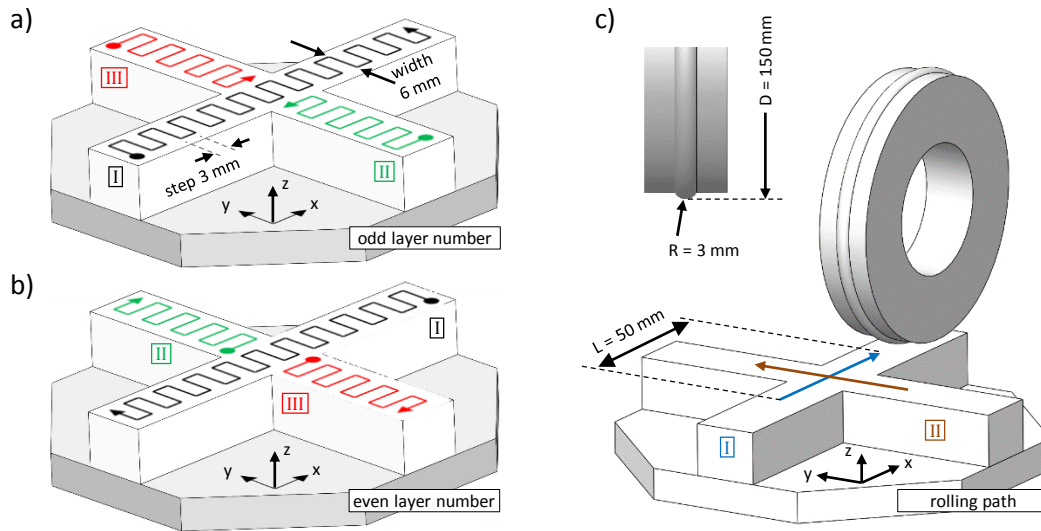
Figure 4: Path strategy for (a) odd and (b) even layers; (c) roller profile and pattern

At the intersection the oscillating width was increased from 6 mm to 10 mm to ensure a neat joint and to provide a near-net-shape with sufficient excess material that allows finish machining. After finishing one pass, the trailing shield remained above the sample for 45 s to prevent oxidation. Even layer numbers were deposited in the opposite direction: the continuous wall (I) was deposited in the negative x-direction and the discontinuous wall (II) & (III) from inside out in negative and positive y-direction respectively. The interlayer dwell time for all four specimens between each layer was 5 min. This allowed cooling and time to manipulate the rolling unit. Two of these four specimens were inter-pass rolled with 75 kN at 5 mm/s rolling speed using a H13 tool steel roller with 150 mm diameter and convex profile of 3 mm radius (Figure 4 c).

Table 1: Deposition Parameters

Current	210	[A]
Torch stand-off	8	[mm]
Travel speed	3.5	[m/min]
Plasma Gas	0.8	[l/min]
Plasma Shield	10	[l/min]
Trailing Shield	~200	[l/min]

Crossing single-pass rolling paths were performed after one intersection layer was completed. The total rolling lengths in both directions was 50 mm and were symmetrical across the intersection (Figure 4 c). Irrespective of whether rolling was applied or not, these deposition parameters produced a total wall width of approximately 10 mm. The build was stopped once the wall reached a height of 25 mm; the last layer had an even layer number. One intersection of each, with and without rolling, was thermally stress relieved, in an inert argon atmosphere at 640 °C for 4 h, while it remained clamped to

the backing block. Finally all four specimens were machined to identical geometries. From the top of the wall, a maximum of 2 mm was machined away to reduce the height to 24 mm. The wall width was machined from approximately 10 mm to 6 mm and the radius at the intersection to 2.5 mm (Figure 5).
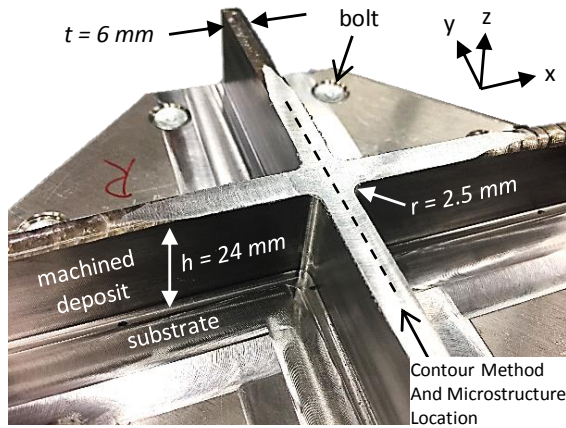

Figure 5: Specimen after Machining

Residual stresses in additive manufacturing are typically measured without finishing processes that potentially influences the stress field, such as machining. However, the neutron path length in the near-net shape would have been 26 mm for the longitudinal and 36.8 mm for the normal direction, which would not have allowed strain measurements in titanium. Finish machining also resulted in a more representative specimen in the condition of operation.

Neutron Diffraction Residual Stress Measurement

Lattice plane spacing measurements for residual stress calculation were carried out at the ENGIN-X time-of-flight neutron diffractometer at the pulsed neutron source of the Rutherford Appleton Laboratory in Didcot, UK [28]. The "white beam" with a wide range of wavelengths close to atomic distances allows the counting of neutrons diffracted by multiple planes simultaneously. Gauge volumes of $3 \times 3 \times 3$ mm^3 were located along the vertical centreline of the specimen with steps of 3 mm. Based on the typical WAAM microstructure [19], [20], it was estimated that 1-10 prior-β grains can be incorporated in the gauge volume. Each of those can contain approximately 10^8 α lamellae, which are estimated to be roughly between 10 μm^3 and 100 μm^3 in size. Their actual size and orientation depend on the orientation and nature of the parent prior-β grain [29] and the cooling rate [30]. Neutron diffraction strain determination requires the measurement of stress-free lattice parameters (d_0) for each location measured. This was

achieved by manufacturing duplicates of each specimen, from which the centre column (5 x 5 x 20 mm) was extracted using electron discharge machining to relieve the residual stresses mechanically. During the d_0 scan, it was established that the texture and sample orientation did not influence the measurement [31]. The specimen was orientated accordingly to obtain measurements in 3 orthogonal directions. Figure 6 (a) shows the setup for the vertical scan during the measurement of the longitudinal x and y directions using two opposite detectors. Figure 6 (b) shows the measurement of the normal direction using the left-hand side detector 1, also called "north bank".
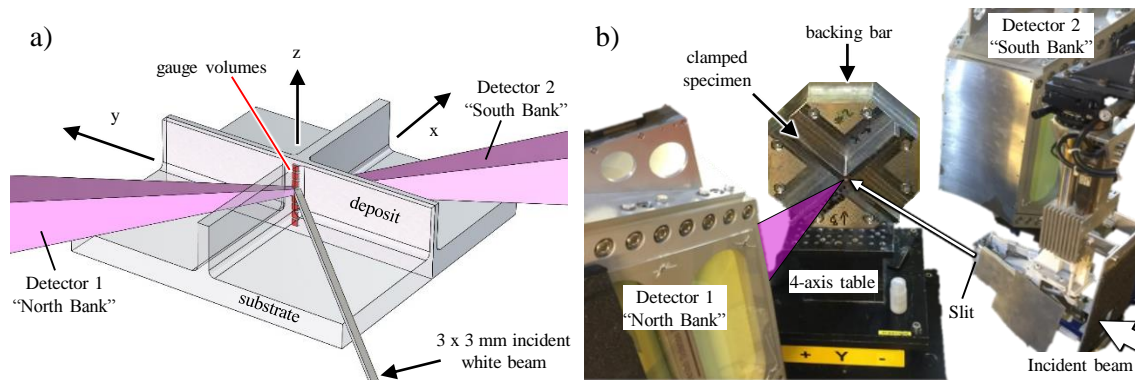

Figure 6: Setup at ENGIN-X: a) Schematic of the beam paths to detect the longitudinal and lateral directions; b) Image of the actual setup on the beam-line to detect the normal plane with the north detector, while the south detector is "dark"

Here the right-hand side detector 2 (or "south bank") remains unused, because the orientation does not align with any of the measured orientations and the neutron path through the titanium substrate plus the thick steel backing bar does not allow the detection of peaks. Machining decreased the path length for the measurement from the values mentioned above of the longitudinal and transverse direction to and 15.5 mm for the normal direction.

In the hexagonal-close-packed (hcp) α crystal, eight planes can be identified within the analysed time-of-flight (TOF) range between 22000 μs and 47500 μs, which are the {2021}, {1122}, {1013}, {1120}, {1012}, {1011}, {0002} and {1010} planes. They were single-peak fitted to determine the plane spacings d and fitted in whole using Pawley refinement [32] to directly determine the hcp lattice parameters a_{hcp} and c_{hcp}. When using monochromatic neutron sources, typically the {1011} or {1013} planes are used to measure strains in Ti-6Al-4V additive manufacturing [6], [33], because they consistently provide good signal strength. In the present study, these two planes were likewise the only ones suitable. Other planes did not diffract in each orientation, which is due to the typical texture: In order to detect a plane, it must align normal to the strain direction to

be measured. Donoghue *et al*. and Antonysamy *et al*. [19], [34], [35] performed electron-backscatter-diffraction (EBSD) measurements to determine the crystallographic α and reconstructed β-orientation in Ti-6Al-4V AM. The procedure to confirm the crystallographic orientation in neutron diffraction using the general materials diffractometer (GEM) at ISIS with EBSD has been performed previously on near-α-titanium [36]. During solidification, the basal $\{100\}_{bcc}$ plane of the high-temperature phase is known to align normal with the build direction z, in other words parallel to the substrate [19], [34], [35]. The Burgers Orientation Relationship (BOR) in Figure 7 (a) shows how the basal $\{0001\}$ α-plane of the bespoke α-lamellae transforms on the $\{110\}_{bcc}$ plane [29] once the temperature drops below the β-transus.

The $\{110\}_{bcc}$ plane has six possible variants in the bcc unit cell, which can be either aligned with the z-axis or hold a 45° angle with it, as shown in Figure 7 (b). According to this and BOR, there are only two possible orientations of the α-crystal in respect to the z-axis, illustrated in Figure 7 (c), which is known from previous EBSD studies on Ti-6AL-4V WAAM [19]. Even with a free rotation around z, some hcp planes can never align with the required global orientation x- or y-direction. When measuring the normal strain, only the $\{11\overline{2}0\}$ or the $\{10\overline{1}2\}$ plane (depending on the $\{110\}_{bcc}$ variant respecting BOR) will align normal with the global z-direction (Figure 7 c), and a rotation around z does not change the relative orientation of either of the planes. Fortunately the $\{10\overline{1}1\}$ or $\{10\overline{1}3\}$ have a small deviation to the $\{10\overline{1}2\}$ plane and can be picked up by the detectors as well. Inter-pass rolling is generally used to improve the mechanical properties in Ti-6Al-4V WAAM. The microstructural effect is the significant reduction in β-grain size from several millimetres to less than 100 μm, as well as the reduction of α colony and lath size [19], [20], which is the phase that is being used for strain measurement in the present work. More important however is the elimination of texture. A larger number of smaller α-grains with a random orientation, caused by inter-pass rolling, facilitates neutron diffraction measurement.
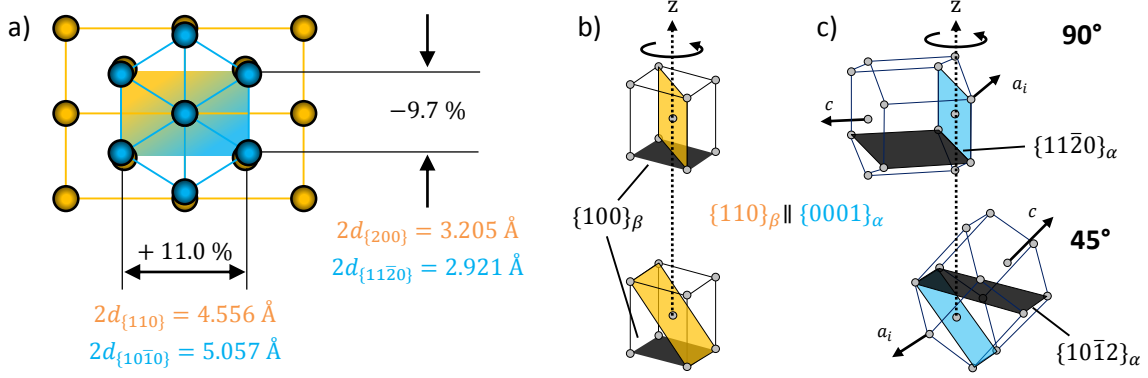
Figure 7: (a) Burgers relationship [37] and change of the lattice during transformation with values taken from the present study; (a) possible orientations of the {110} variants; (a) possible orientations of the hcp unit cell after transformation.

For a consistent residual stress evaluation of all specimens, only the stress calculation based on the single-peak-fitted {1011} and {1013} planes were used, as Pawley refinement is only compatible with the rolled specimen that diffracts all peaks. Lattice strain and residual stress in the three principal directions were calculated using eq. (1) and (2). ε_{ii} is the strain in the respective orientation, based on a specific crystallographic plane d_{hkl}. σ_{ii} is the calculated stress in the corresponding direction [38]; It was attempted to calculate the stress based on as many planes as possible using the individual elastic constants E_{hkl} and ν_{hkl}. Stapleton *et al.* [39] have measured the Young's moduli for six different α-planes and derived the single-crystal elastic constants $\boldsymbol{C_{ij}}$ from them, which allows the completion of the full stiffness matrix $\underline{C}$ and its inverse, the compliance matrix $\underline{S}$. However only the {1011} and the {1013} planes were suitable for stress calculation (E_{1011} = 98 GPa and E_{1013} = 105 GPa), which was only clear after the data analysis. The Poisson ratio used for both planes was ν = 0.342 [40]. The uncertainty for the strain and stress values were calculated with eq. (4) and (5), based on the partial differential eq. (3) for the propagation of uncertainty, using the uncertainty Δd_{hkl} of the single peak fit.

$$\varepsilon(d_{hkl})_{ii} = \frac{d_{hkl} - d_{hkl,0}}{d_{hkl,0}} \tag{1}$$

$$\sigma_{ii} = \frac{\nu_{hkl}E_{hkl}}{(1 + \nu_{hkl})(1 - 2\nu_{hkl})}\left(\varepsilon_{xx} + \varepsilon_{yy} + \varepsilon_{zz}\right) + \frac{E_{hkl}}{1 + \nu_{hkl}}\varepsilon_{ii} \tag{2}$$

$$\Delta y = \sum_{i=1}^{n}\left|\frac{\partial f}{\partial x_i} * \Delta x_i\right| \tag{3}$$

$$\Delta\varepsilon = \left(\frac{1}{d_0}\right) * \Delta d + \left(-\frac{d}{d_0^2}\right) * \Delta d_0 \tag{4}$$

$$\Delta\sigma_{ii} = \frac{vE}{(1+v)(1-2v)}\left(\Delta\varepsilon_{xx} + \Delta\varepsilon_{yy} + \Delta\varepsilon_{zz}\right) + \frac{E}{1+v}\Delta\varepsilon_{ii} \qquad (5)$$

Contour Method

After the non-destructive neutron experiments the contour method was performed for residual stress analysis. A Fanuc Robocut α-C600i EDM machine was used to cut the specimen in a deionised water bath, while the specimen remained clamped on the 36-mm-thick backing bar. 250-μm-diameter brass wire was used to perform the contour cut, oriented parallel to the y-axis and located in the symmetry plane of the intersection, as indicated with the dashed line in Figure 5. The cut was performed in the negative z-direction from the top to the bottom of the specimen, thereby cutting through the location of the neutron gauge volume locations to give a direct comparison. As soon as the contour cut was completed and the wire entered the backing bar, the cut was stopped and both halves of the specimen were removed from the backing bar. This is unconventional procedure and does not satisfy the zero-net-stress assumption. It was chosen with the attempt to measure the as-deposited stress before unclamping and consequent distortion (to be comparable with the neutron diffraction result). After ultrasonic cleaning, the surface displacement of both cut halves were measured in a temperature-controlled room on a Zeiss Contura g2 coordinate measuring machine (CMM) with 3-mm-diameter ruby touch probe with a step size of 0.5 mm. The topographical data cloud from both cut surfaces of the samples was processed with Matlab analysis routines for data aligning, cleaning, flattening and smoothing [41]. For smoothing, a cubic spline with a knot spacing of 5.5 mm in both directions was used. For the finite element (FE) analysis one cut half of the sample was modelled in Abaqus software using an 8-node brick element and a uniform mesh with 1 mm distance between the adjacent FE nodes. The stress calculation was based on the linear elastic properties E = 114 GPa and v = 0.342.

Microstructure

Optical microstructural analysis was performed on the surface of the contour cut at the location of the neutron gauge on the as-deposited and the inter-pass-rolled specimens (dashed line in Figure 5). Conventional sample preparation including grinding, polishing

and etching with hydrofluoric acid exposed the microstructure, which was then analysed using an optical microscope with 50x magnification.

3 Results

Microstructure

Figure 8 (a) and (b) compare the cross-sectional Ti-6Al-4V microstructures in the additively manufactured intersections of the as-deposited and the inter-pass-rolled specimen. The location and size of the first and last ND gauge volumes are shown in their actual location and size.
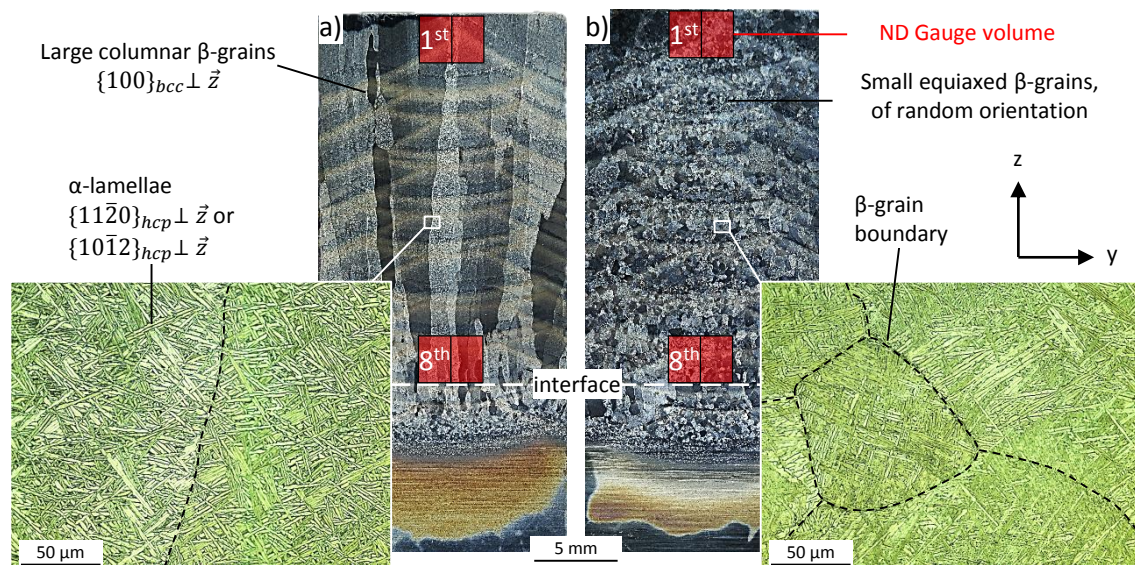

Figure 8: Microstructure in the neutron diffraction gauge volume located on the contour cut surface (YZ) of (a) the as-deposited sample with large columnar prior-β grains containing hcp α-lamellae; the hcp cell is oriented according to Figure 7 and [29]; (b) the inter-pass rolled sample with very small, round and equiaxed prior-β grains containing smaller hcp α-lamellae. The identical horizontal bowed lines are the layer bands (or HAZ).

Large columnar prior-β grains are visible in the as-deposited specimen (Figure 8 a) and only a few are incorporated by the neutron gauge volume. The high magnification image is located on a prior-β grain boundary, showing the α-lamellae organised in the typical basketweave fashion. Alignment constraints of the hcp α-crystal in respect to the orientation of the lamellae and prior-β grain boundary was discussed by Mathisen *et al*. [29]. Inter-pass rolling produced the expected fine and equiaxed prior-β microstructure (Figure 8 b), of which approximately 5000 populate the neutron gauge volume and each of those contain a large number of α-lamellae. The high magnification shows a 100-μm-diameter grain. Inside developed α-lamellae that are smaller compared to the as-deposited microstructure. The random orientation and large number of prior β-grains however imparts its untextured morphology to the incorporated α-phase. The identical

pattern of the heat-affected zones in both specimen (HAZ) highlights the similarity of the thermal history, showing that the smaller α-lamellae are not due to a faster cooling rate.

Neutron Diffraction

Figure 9 shows typical spectra in the longitudinal and the normal configuration of the as-deposited and the inter-pass-rolled d_0 measurements. Planes with similar behaviour are shown in the same colour-scheme consistently through this paper. The intensities of the actual specimens were lower, due to the increased path length. The inter-pass rolled specimen did not show significant texture, whereas the diffraction pattern of the as-deposited specimen showed a highly orientation-dependent behaviour.
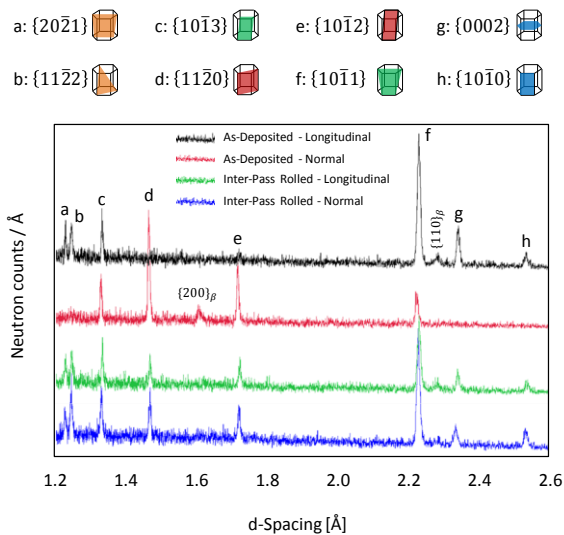
a: $\{20\bar{2}1\}$ c: $\{10\bar{1}3\}$ e: $\{10\bar{1}2\}$ g: $\{0002\}$

b: $\{11\bar{2}2\}$ d: $\{11\bar{2}0\}$ f: $\{10\bar{1}1\}$ h: $\{10\bar{1}0\}$

Figure 9: Exemplary fitted spectra of longitudinal and normal directions of as-deposited and inter-pass rolled samples.

The $\{1120\}$ and the $\{1012\}$ planes (red) did not show a peak in the longitudinal direction of the as-deposited sample, but they were the strongest peaks in the normal direction. In turn, the basal $\{0002\}$ plane and the prismatic $\{1010\}$ plane (blue) were relatively strong in the longitudinal direction, but c vanished in the normal direction. This is in agreement with the theory, because the z-rotation of the unit cells, which only occur in the two variants shown in Figure 7 (c), does not allow the geometrical alignment of some planes with global orientations. Table 2 compares the measured plane spacings with the expected detectability of α-planes according to the typical texture and BOR, as explained in the methodology section. Also detected were the $\{110\}_{bcc}$ plane in the longitudinal direction and the $\{200\}_{bcc}$ plane in the normal direction, confirming the prior-β orientation.

Table 2: Theoretical and experimental detection of hcp-planes in Ti-6Al-4V WAAM with the typical strong prior β texture

		{20$\bar{2}$1}	{11$\bar{2}$2}	{10$\bar{1}$3}	{11$\bar{2}$0}	{10$\bar{1}$2}	{10$\bar{1}$1}	{0002}	{10$\bar{1}$0}
Longitudinal direction (x & y)	90° hcp orient.	good		good			good	good	good
	45° hcp orient.	good		good			good		
	Experimental	moderate	moderate	good			very good	good	good
Normal direction (z)	90° hcp orient.			moderate	very good		moderate		
	45° hcp orient.					very good			
	Experimental			good	very good	very good	good		

All stress-free lattice parameters d_0 were found to be isotropic and independent from their location in the wall or whether the wall was inter-pass rolled or not. Table 3 shows the determined stress-free d_0 of all detected planes of both detectors, as well as the magnitude of fit uncertainty absolute and in strain. Throughout all conditions the {1011} was fitted with the smallest error. Thermal stress relieving slightly decreased the plane spacings by 2.3×10^{-4} Å on average. Throughout all measurements, the north detector measured a d-spacing of approximately 4×10^{-4} Å more than the one measured by the south detector. Therefore each strain was calculated by comparing the strained d-values against the d_0 measured by the same detector to take detector errors into account.

Table 3: Stress free d-spacings of the hcp α-phase

		{20$\bar{2}$1}	{11$\bar{2}$2}	{10$\bar{1}$3}	{11$\bar{2}$0}	{10$\bar{1}$2}	{10$\bar{1}$1}	{0002}	{10$\bar{1}$0}
As-deposited	d_north [Å]	1.22075	1.23781	1.32506	1.46095	1.71492	2.22392	2.33436	2.52858
	fit uncert. [10^{-4} Å]	2.6	1.9	1.8	2.2	2.2	1.1	2.4	4.3
	fit uncert. [x10^-6]	203.0	153.5	135.8	150.6	128.3	49.5	102.8	170.1
	d_south [Å]	1.22010	1.23746	1.32463	1.46090	1.71484	2.22352	2.33385	2.52817
	fit uncert. [10^{-4} Å]	2.3	1.8	2.1	1.9	2.2	1.1	2.2	3.9
	fit uncert. [x10^-6]	188.5	145.5	158.5	130.1	128.3	49.5	94.3	154.3
Stress relieved	d_north [Å]	1.22063	1.23784	1.32480	1.46060	1.71464	2.22375	2.33349	2.52846
	fit uncert. [10^{-4} Å]	2.2	1.8	1.5	1.3	1.4	0.8	2.1	3.4
	fit uncert. [x10^-6]	180.2	145.4	113.2	89.0	81.6	36.0	90.0	134.5
	d_south [Å]	1.22003	1.23740	1.32449	1.46043	1.71444	2.22336	2.33343	2.52827
	fit uncert. [10^{-4} Å]	1.7	1.5	1.5	1.5	1.6	0.8	1.6	3.2
	fit uncert. [x10^-6]	139.3	121.2	113.3	102.7	93.3	36.0	68.6	126.6

The diagrams in Figure 10 show the strain profiles in the three orthogonal directions for the as-deposited and inter-pass-rolled specimens from those planes that gave a diffraction pattern, as well as the strain of the lattice parameters a_{hcp} and c_{hcp} using the Pawley refinement for comparison. The profiles from the different planes are comparable. The {1120}, {1012}, {0002} and {1010} planes sometimes diverge from the other profiles. In particular, the a and c strain values in the normal direction of the as-deposited specimen diverge dramatically from the other planes and each other (Figure 10 c). Finally only the {1011} and {1013} planes (green) were used for stress calculation. Error bars are not displayed intentionally to preserve clarity, however the uncertainty of the measurements were approximately factor 2 to 3 compared to those of the d_0 in Table 3. The average strain uncertainties for the {1011} and {1013} planes for example were 101×10^{-6} and 269×10^{-6} respectively.
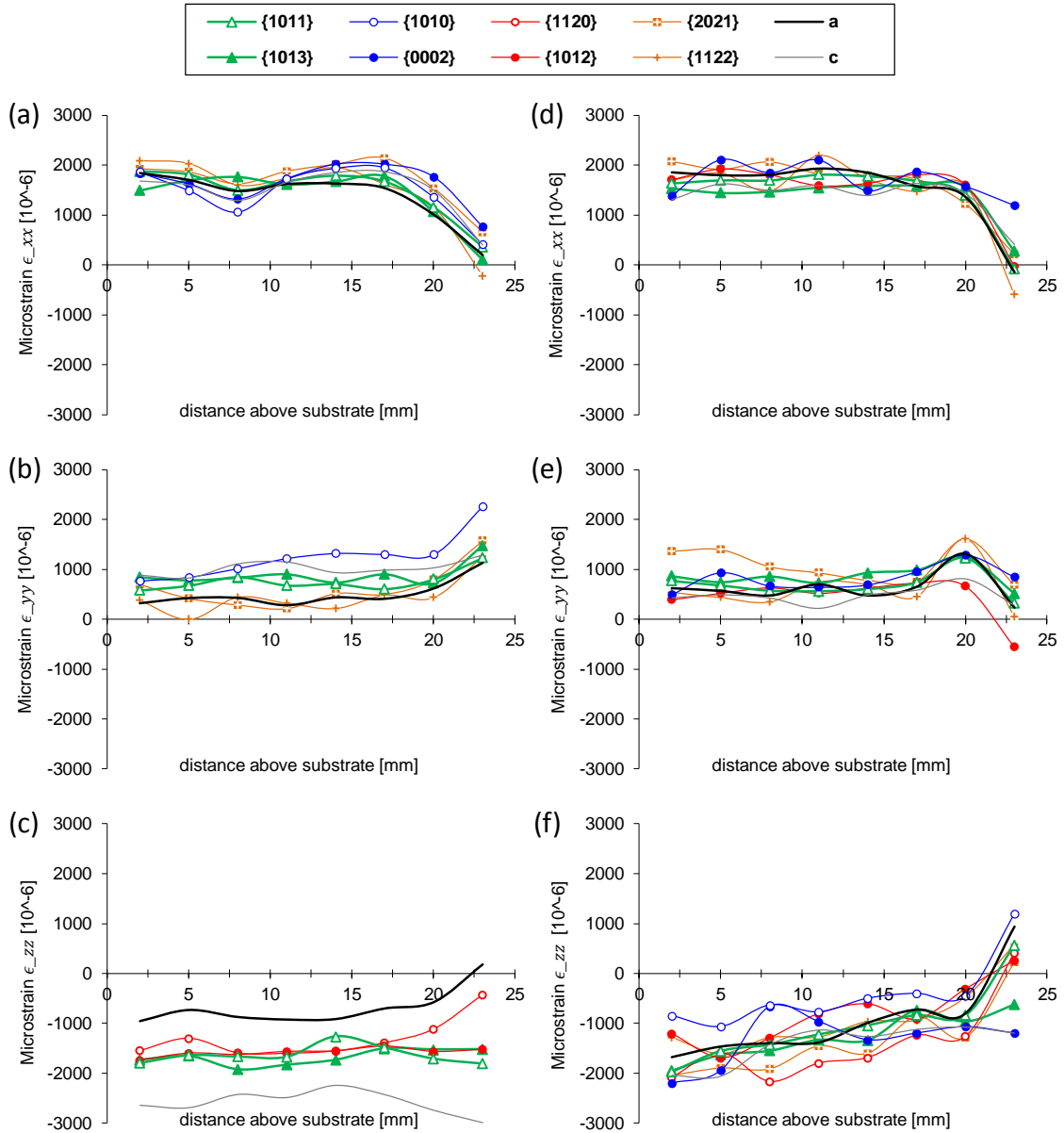
Figure 10: Residual strain profile along the symmetry line in all three principle directions of the as-deposited sample in (a) x, (b) y and (c) z direction; and of the and inter-pass rolled sample in (d) x, (e) y and (f) z direction.

Figure 11 (a-c) shows the averaged residual stresses of the {1011} and {1013} planes in (a) the longitudinal x, in (b) the transverse y and (c) the normal z-directions. The relatively high uncertainty is due to the weaker signal strength of the measurements compared to the d_0 (Figure 9). However, the good point-to-point consistency in all profiles increases confidence. The longitudinal residual stress profile in the x-direction of the as-deposited specimen is constant along the height at approximately 200 MPa and drops to almost zero towards the top of the specimen. In the transverse y-direction the stress is constant along the height at approximately 100 MPa, but without the drop at the top. The inter-pass-rolled specimen has similar profiles, with slightly larger values in both directions. The only difference is the drop in tensile stress in the top region of

the transverse direction, caused by the last rolling step. The stress-relieved specimens did not contain significant residual stresses in any direction. The longitudinal stresses are slightly tensile, while the normal stresses are slightly compressive. Noteworthy is the tensile region in the upper half of the inter-pass rolled specimen in the normal direction while the as-deposited one is effectively stress-free or slightly compressive.
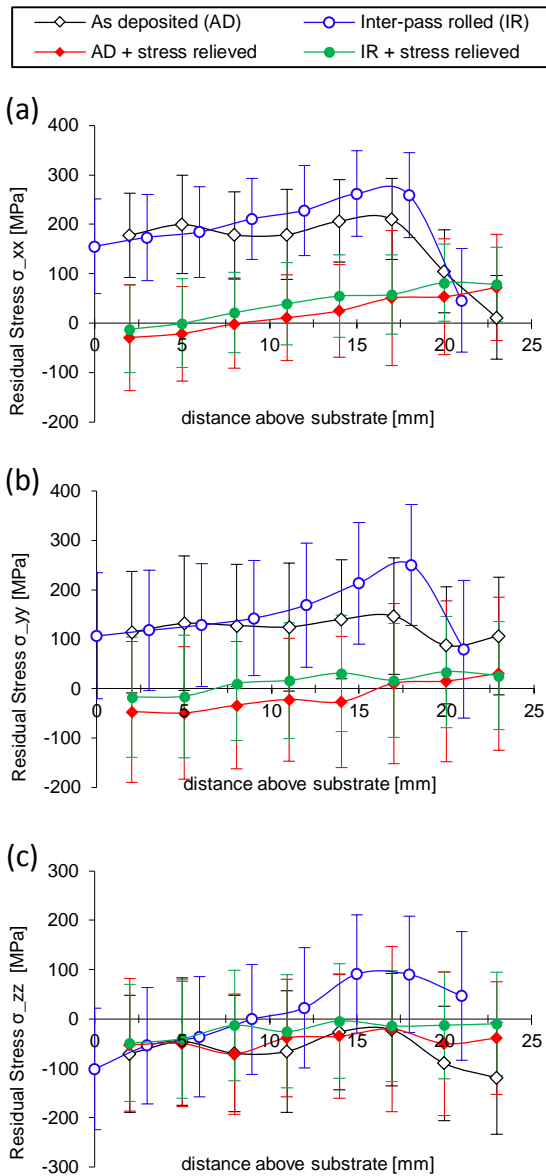

Figure 11: Calculated average orthogonal residual stresses using neutron diffraction with the {1011} and {1013} planes in the (a) longitudinal, the (b) transverse and (c) the normal directions.

Contour Method

Figure 12 shows the residual stress maps in the y-z plane for all four specimens. Both the non-heat-treated specimens (as-deposited (a) and inter-pass rolled (b)) have virtually identical residual stress maps. At the top centre both have a small region of very large compressive stress, reaching -356 MPa and -313 MPa respectively. Large tensile

stresses can be seen below the interface, where they are the largest just under the intersections at 338 MPa and 325 MPa. Further balancing compressive regions are located at the wide edges and the bottom of the substrate. The through-thickness stress in the lateral deposit (on the left and the right side of the longitudinal deposit) is practically zero.
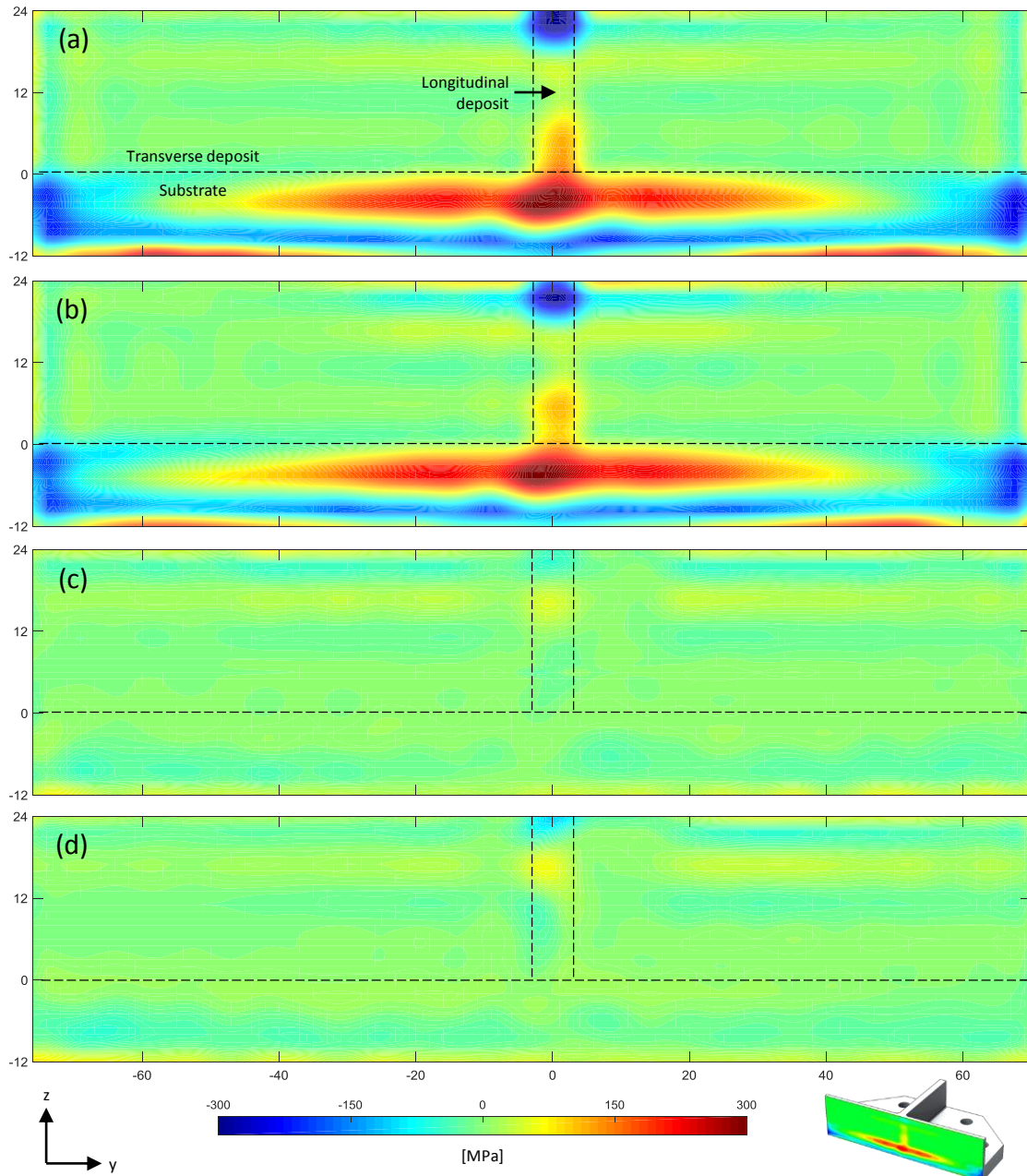

Figure 12: Full residual stress maps produced by the contour method on the y-z plane of all four specimens: (a) as deposited and (b) inter-pass rolled and both after stress-relieving (c, d); units in [mm]; horizontal and vertical dashed lines indicate the interface with the substrate and the wall contour respectively.

The only noteworthy difference of the as-deposited and the inter-pass rolled stress map is the slightly increased compressive region under the rolled length in the inter-pass rolled specimen, revealing little impact of the cold work on the residual stresses in

general. Both stress-relieved specimens (Figure 12 c and d) are virtually stress-free, as they range between -32 MPa and 20 MPa. Only the strong compressive field at the top of the intersection and the balancing tensile field just below were not relieved entirely.

4 Discussion

Neutron Diffraction

Ti-6Al-4V is an α+β alloy. The low-temperature hcp α-phase completes the transformation into full body-centred cubic (bcc) β-phase at approximately 995 °C [37]. The moderate-to-fast cooling rates resulted in the formation of a fully lamellar microstructure, in which the α-lamellae start growing from the parent β grain boundary, as shown in Figure 8 (a). These lamellae are separated by a small residual β phases and can form a colonies within the parent β grain [42], [43]. At room temperature Ti-6Al-4V typically contains between 3% and 9% of the high-temperature β-phase [25], [44] and non-instantaneous cooling allows partitioning, which in this case is the diffusion of Al and V into the respective phase that they stabilise. This influences the lattice parameters of both hcp and bcc unit cells [45]–[47]. Elmer *et al.* [48] reported no diffusion or change in lattice size up to 550 °C. However, above a stress relieving temperature of 600 °C the lattice size can change, but this was observed in a non-lamellar, equiaxed-like and oversaturated Ti-6Al-4V microstructure with 12.1 % β-phase prior to stress relieving. This may have allowed diffusion and lattice change at a lower temperature, while no significant lattice size change was observed in the present study. Furthermore the rapid cooling rate used by Elmer *et al.* [48] retained homogenised elements in the matrix and did not allow partitioning after heat treatment, while the slow furnace cooling during the stress relief of the intersections could have reset the initial lattice size.

Inter-pass rolling changes the microstructure significantly, as shown in Figure 8 (b). The stress-free lattice parameter however did not change within the resolution of ENGIN-X, suggesting a comparable composition in the α-phase, regardless of the reduced α-lamellae size and reorientation. Hence rolling did not influence the composition (i.e. partitioning) at identical thermal histories. The argument is supported by the similar appearance of the HAZ (Figure 8 (a, b), which is evidence for a similar thermal cycle.

Furthermore, rolling did not make any significant difference to the final residual stress state. Hence the thermal history must have been dominant. However rolling had a

positive impact on the material texture, as it reduced the preferred orientation and size of α and β grains and thereby allowing the detection of all hcp planes during the neutron measurements, so exploiting the potential of the white beam at ENGIN-X. This reduced texture and grain sizes are known to improve the mechanical properties [20], [21].

Stress Development in intersections

In comparison to previous work, where the longitudinal residual stress in a single free-standing Ti-6Al-4V WAAM wall reached 500 MPa [3], [6], [33], [49], the residual stress in the intersection was, at 200 MPa, significantly lower. Two reasons could be that the total longitudinal (and transverse) length of the wall was 150 mm, which is shorter than the samples reported in the literature or finish machining might have released tensile residual stresses. A third reason could be the oscillating path strategy, which has a comparably high energy input per unit length, resulting in a higher component temperature and smaller temperature gradient. A final explanation could be the self-stress-relieving nature of intersections, determined by the path strategy and sequence of passes. This phenomenon was observed previously in an numerical simulation that predicted less residual stresses in the intersection, compared to the longitudinal tensile stresses in the adjacent free-standing walls [23]. This suggests that the reason is due to the thermal strategy, rather than machining. Figure 13 illustrates the residual stress development during the deposition of a single intersection layer, generated by three subsequent intersecting passes.
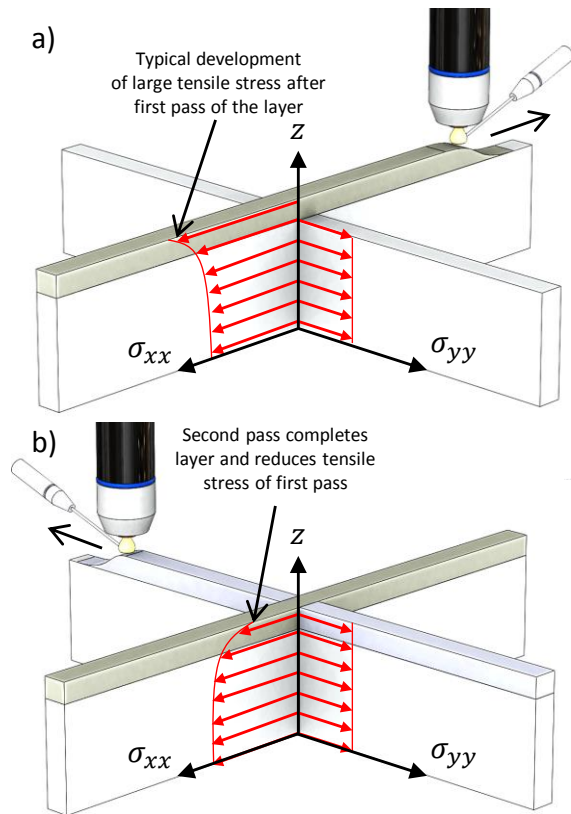
Figure 13: Longitudinal tensile residual stress development in additively manufactured intersections showing (a) the tensile stress build up in a deposit and its relieve (b), once the lateral pass is deposited.

The first pass of the continuous intersection layer presumably generates typical longitudinal tensile residual stresses (Figure 13 a). The following laterally-deposited pass completes the layer (Figure 13 b). Thermal shrinkage also results in the development of tensile residual stress in the longitudinal direction, but it also effects the previous deposition, as the through-thickness shrinkage of the second pass is constrained by the intersection. The through-thickness shrinkage of the second pass compresses the first pass longitudinally and therefore counteracts the previously developed tensile stress. The established residual stress profile along the additively manufactured intersection is therefore tensile in both directions and constant along the height, larger in the direction of the continuous wall, but still lower than in a free-standing wall. The steep drop in stress at the top in x-direction is therefore caused by the second pass in y-direction. A similar observation was made in simulations of intersections [23]. The stress profile in the normal direction is close to zero or slightly compressive, which averts development of possible hydrostatic tensile stresses. The second and third gauge volume from the top of the inter-pass rolled specimen however do show low but potentially problematic

hydrostatic tensile stress with a minimum of 100 MPa. This is an effect that was also observed in rolling of free-standing single pass walls [4].

The residual stress profile as-deposited, which is strongly tensile in two directions and near zero or slightly compressive in the third direction can be thermally stress-relieved. The achieved residual stress of a little less than 100 MPa was still larger than expected [8] using the stress relieving temperature of 650 °C, hence little residual distortion after unclamping was observed. A higher stress relieving temperature would further reduce the stresses [8] but could involve a microstructural modification at and above 700 °C.

Contour Method

The contour method is normally performed on a free-standing specimen without superimposed external clamping loads. When post-processing the topography of a contour surface, the net-stress on that cross section is assumed to be zero. However, in the present study the substrate remained clamped onto the backing bar, maintaining significant clamping loads in the specimen, so the cross-sectional residual stress was not self-balanced. The zero-stress assumption for the contour method is therefore no longer valid. Figure 14 shows the comparison of the neutron diffraction results with the equivalent profile taken from the contour stress map. The difference originates from the contour cut traversing through the unbalanced stress field: neutron diffraction measurement show large tensile stresses along the height of the specimen (Figure 11 (a, b)), as is also known for the clamped condition in single pass walls [6], [50]. The relatively large area on both sides from that location is expected to contain very little stress normal to the cut surface, as this stress represents the through-thickness stress of the lateral deposits. The backing bar in turn must contain balancing compressive stresses. As the contour cut propagates in a negative z-direction through the specimen, tensile stressed material is removed continuously, which in turn reduces the balancing compressive stresses in the substrate. Once the contour cut has passed through the entire cross section of the specimen, the tensile stresses on the y-z plane are removed and the backing bar will no longer carry a balancing compressive stress. Based on the incomplete cut through one component of the assembly two explanations for the deviation from the contour method to neutron diffraction are possible, as follows.

The balancing stresses in the backing bar are responsible for the discrepancy between the neutron and contour results, as they offset the contour cut surface from the net-zero assumption. This offset decreases continuously as the contour cut propagates until it reaches the interface between specimen and backing bar. Comparing the stresses obtained by the two methods from the as-deposited and the inter-pass rolled specimen in Figure 14 (a, b) shows the continuously decreasing mismatch from the top of the specimen to the interface. Figuratively, performing the contour cut on the clamped specimen is effectively continuously unclamping it and therefore suggests a stress-profile that appears like the profile of an unclamped wall compared to a clamped wall (Figure 1).

Furthermore the zero stress assumption is not valid in any case and requires post-processing for a better understanding. The difference in the stress-relieved specimen between the contour method and neutron diffraction Figure 14 (c, d) is smaller, because the EDM cutting error would be reduced by stress relieving.

The slight waviness in the stress plots taken from the contour method can be attributed to the spline fit, as half the wavelength is equivalent to the knot spacing in the spline fit. This waviness is also evident on both directions in the contour map in Figure 12. Plasticity has been reported to play a role when the stresses are either above or close to the material yield strength, however with a typical longitudinal yield strength of 850 MPa [22] plasticity is not expected to be an issue.
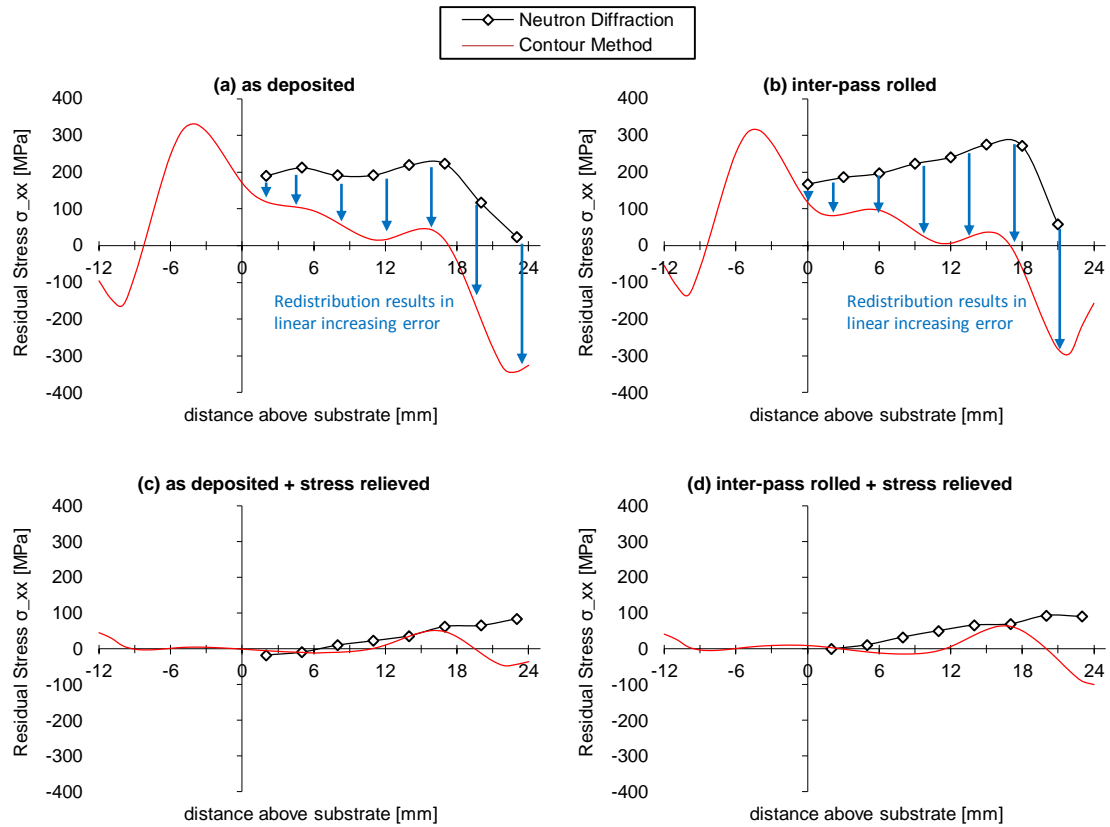
Figure 14: Comparison of the neutron diffraction experiment of the as-deposited (a) and inter-pass rolled specimen (b) and both after stress relieving (c, d).

Nevertheless, comparing the as-deposited and inter-pass rolled contour maps (Figure 12 (a, b)) shows that rolling did not influence the residual stresses and the location of most critical stress can be identified with confidence at the root of the deposit, and especially at the intersection. Finally the stress-relieved contour maps suggest a successful stress relief without any stress gradients (Q.E.D) and agrees with the neutron diffraction results.

5   Conclusions

In this study the effect of vertical inter-pass rolling and thermal stress relieving on Ti-6Al-4V intersections produced by Wire + Arc Additive Manufacturing has been investigated. We have demonstrated that:

1. The as-deposited material shows a strong crystallographic texture, which can be virtually eliminated by inter-pass rolling. As deposited, only the {1011} and {1013} planes diffract consistently neutrons in all three assumed principal directions in Ti-6Al-4V WAAM. As a consequence Pawley refinement is unsuitable for stress calculation. It only becomes suitable when the texture is eliminated and the prior-β grains are significantly refined.

2. Hydrostatic tensile stresses were not found in the as-deposited intersection, hence thermal stress-relieving significantly reduced the residual stress. The inter-pass rolled intersection contained low hydrostatic stress below the plastically deformed region of the last rolling step, but it did not limit the thermal stress relieving at this location. However, inter-pass rolling did not have any other effect on the residual stresses.

3. The residual stress in the intersections is tensile in the longitudinal directions of both walls and constant along the height. The stress in the continuously deposited wall is higher than in the discontinuous one. After the first and continuous deposition of the intersection, the subsequent transverse deposit, which completes the layer, diminishes the residual stress of the previous deposit. Normal stresses are relatively constant along the wall height as well, but compressive.

4. The zero-stress assumption for the contour method is not valid in this unbalanced stress field and requires post-processing. Nevertheless the contour method results reveal qualitatively the regions of large stresses and gradients in as-deposited intersections and furthermore suggest that thermal stress relieving can eliminate residual stresses in AM intersections entirely.

References

[1]   S. W. Williams, F. Martina,   a. C. Addison, J. Ding, G. Pardal, and P. Colegrove, "Wire+Arc Additive

Manufacturing," *Mater. Sci. Technol.*, vol. 32, no. 7, pp. 641–647, 2015.

[2]   F. Martina, M. Roy, P. Colegrove, and S. Williams, "Residual Stress Reduction in High Pressure Interpass Rolled Wire + Arc Additive Manufacturing Ti-6Al-4V components," in *25th International Solid Freeform Fabrication*, 2014, pp. 89–94.

[3]   P. A. Colegrove, F. Martina, M. J. Roy, B. Szost, S. Terzi, S. W. Williams, P. J. Withers, and D. Jarvis, "High pressure interpass rolling of Wire + Arc Additively Manufactured titanium components," *Adv. Mater. Res.*, vol. 996, pp. 694–700, 2014.

[4]   P. A. Colegrove, H. E. Coules, J. Fairman, F. Martina, T. Kashoob, H. Mamash, and L. D. Cozzolino, "Microstructure and residual stress improvement in wire and arc additively manufactured parts through high-pressure rolling," *J. Mater. Process. Technol.*, vol. 213, pp. 1782–1791, 2013.

[5]   J. Ding, P. Colegrove, J. Mehnen, S. Williams, F. Wang, and P. S. Almeida, "A computationally efficient finite element model of wire and arc additive manufacture," *Int. J. Adv. Manuf. Technol.*, vol. 70, pp. 227–236, 2014.

[6]   J. R. Hönnige, S. Williams, M. J. Roy, P. Colegrove, and S. Ganguly, "Residual Stress Characterization and Control in the Additive Manufacture of Large Scale Metal Structures," in *10th International Conference on Residual Stresses*, 2016.

[7]   H. E. Coules, "Contemporary approaches to reducing weld-induced residual stress," *Mater. Sci. Technol.*, vol. 29, no. 1, 2012.

[8]   Z. Wang, A. D. Stoica, D. Ma, and A. M. Beese, "Stress relaxation behavior and mechanisms in Ti-6Al-4V determined via in situ neutron diffraction: Application to additive manufacturing," *Mater. Sci. Eng. A*, no. Accepted Manuscript, 2017.

[9]   G. Longhitano, M. Aparecida, A. Jardini, C. de Carvalho, and M. Filippini, "Correlation between microstructures and mechanical properties under tensile and compression tests of heat-treated Ti-6Al – 4 V ELI alloy produced by additive manufacturing for biomedical applications," *J. Mater. Process. Tech.*, vol. 252, no. November 2016, pp. 202–210, 2018.

[10]   H. Galarraga, R. J. Warren, D. A. Lados, R. R. Deho, M. M. Kirka, and P. Nandwana, "Effects of heat treatments on microstructure and properties of Ti-6Al-4V ELI alloy fabricated by electron beam melting (EBM)," *Mater. Sci. Eng. A*, vol. 685, pp. 417–428, 2017.

[11]   N. Hrabe, T. Gnaupel-Herold, and T. Quinn, "Fatigue properties of a titanium alloy (Ti-6Al-4V) fabricated via electron beam melting (EBM): Effects of internal defects and residual stress," *Int. J. Fatigue*, vol. 94, pp. 202–210, 2017.

[12]   L. E. Murr, "Metallurgy of additive manufacturing: Examples from electron beam melting," *Addit. Manuf.*, vol. 5, pp. 40–53, 2015.

[13]   A. Jurcius, A. V. Valiulis, O. Cernasejus, K. J. Kurzydlowski, A. Jaskiewicz, and M. Lech-Grega, "Influence of vibratory stress relief on residual stresses in weldments and mechanical properties of structural steel joint.pdf," *J. Vibroengineering*, vol. 12, no. 1, pp. 133–141, 2010.

[14]   V. Fartashvand, A. Abdullah, and S. A. S. Vanini, "Ultrasonics Sonochemistry Investigation of Ti-6Al-4V alloy acoustic softening," *Ultrason. - Sonochemistry*, vol. 38, pp. 744–749, 2017.

[15]   V. I. Kurkin, S. A., Anufriev, "Preventing distortion of welded thin-walled members of AMg6 and 1201 aluminum alloys by rolling the weld with a roller behind the welding arc," *Sverochnoe Proizv.*, vol. 31, no. 10, pp. 52–55, 1984.

[16]   J. Altenkirch, A. Steuwer, P. J. Withers, S. W. Williams, M. Poad, and S. W. Wen, "Residual stress engineering in friction stir welds by roller tensioning," *Sci. Technol. Weld. Join.*, vol. 14, no. 2, pp. 185–192, 2009.

[17]   D. F. O. Braga, H. E. Coules, T. Pirling, V. Richter-Trummer, P. Colegrove, and P. M. S. T. De Castro, "Assessment of residual stress of welded structural steel plates with or without post weld rolling using the contour method and neutron diffraction," *J. Mater. Process. Technol.*, vol. 213, no. 12, pp. 2323–2328, 2013.

[18]   H. E. Coules, P. Colegrove, L. D. Cozzolino, S. W. Wen, S. Ganguly, and T. Pirling, "Effect of high pressure rolling on weld-induced residual stresses," *Sci. Technol. Weld. Join.*, vol. 17, no. 5, pp. 394–401, 2012.

[19]   J. Donoghue, A. A. Antonysamy, F. Martina, P. A. Colegrove, S. W. Williams, and P. B. Prangnell, "The effectiveness of combining rolling deformation with Wire-Arc Additive Manufacture on β-grain refinement and texture modification in Ti-6Al-4V," *Mater. Charact.*, vol. 114, pp. 103–114, 2016.

[20]   F. Martina, P. A. Colegrove, S. W. Williams, and J. Meyer, "Microstructure of Interpass Rolled Wire + Arc Additive Manufacturing Ti-6Al-4V Components," *Metall. Mater. Trans. A Phys. Metall. Mater. Sci.*, vol. 46, no. 12, pp. 6103–6118, 2015.

[21] F. Martina, S. W. Williams, and P. Colegrove, "Improved microstructure and increased mechanical properties of additive manufacture produced Ti-6Al-4V by interpass cold rolling," *SFF Symp.*, pp. 490–496, 2013.

[22] P. A. Colegrove, J. Donoghue, F. Martina, J. Gu, P. Prangnell, and J. Hönnige, "Application of bulk deformation methods for microstructural and material property improvement and residual stress and distortion control in additively manufactured components," *Scr. Mater.*, vol. 2, 2016.

[23] J. Mehnen, J. Ding, H. Lockett, and P. Kazanas, "Design study for wire and arc additive manufacture Jörn Mehnen * and Jialuo Ding Panos Kazanas," *Int. J. Prod. Dev.*, vol. 19, no. 1–3, pp. 2–20, 2014.

[24] M. B. Prime, "Cross-Sectional Mapping of Residual Stresses by Measuring the Surface Contour After a Cut," *J. Eng. Mater. Technol.*, vol. 123, no. April 2001, p. 162, 2001.

[25] J. J. Lin, Y. H. Lv, Y. X. Liu, B. S. Xu, Z. Sun, Z. G. Li, and Y. X. Wu, "Microstructural evolution and mechanical properties of Ti-6Al-4V wall deposited by pulsed plasma arc additive manufacturing," *Mater. Des.*, vol. 102, no. 102, pp. 30–40, 2016.

[26] J. Ding, P. Colegrove, F. Martina, S. Williams, R. Wiktorowicz, and M. R. Palt, "Development of a laminar flow local shielding device for wire+arc additive manufacture," *J. Mater. Process. Technol.*, vol. 226, pp. 99–105, 2015.

[27] A. Caballero, "Discolouration of Titanium in Wire and Arc Additive Manufacturing," Cranfield University, 2015.

[28] J. R. Santisteban, M. R. Daymond, J. A. James, and L. Edwards, "ENGIN-X: A third-generation neutron strain scanner," *J. Appl. Crystallogr.*, vol. 39, no. 6, pp. 812–825, 2006.

[29] M. Borlaug Mathisen, L. Eriksen, Y. Yu, O. Jensrud, and J. Hjelen, "Characterization of microstructure and strain response in Ti-6Al-4V plasma welding deposited material by combined EBSD and in-situ tensile test," *Trans. Nonferrous Met. Soc. China (English Ed.*, vol. 24, no. 12, pp. 3929–3943, 2014.

[30] B. K. Foster, A. M. Beese, J. S. Keist, E. T. Mchale, and T. A. Palmer, "Impact of Interlayer Dwell Time on Microstructure and Mechanical Properties of Nickel and Titanium Alloys," *Metall. Mater. Trans. A*, vol. 48, no. 9, pp. 4411–4422, 2017.

[31] T. M. Holden, Y. Traore, J. James, J. Kelleher, and P. J. Bouchard, "short communications Determination and mitigation of the uncertainty of neutron diffraction measurements of residual strain in large-grained polycrystalline material," pp. 582–584, 2015.

[32] G. S. Pawley, "Unit-cell refinement from powder diffraction scans," *J. Appl. Crystallogr.*, vol. 14, p. 357, 1981.

[33] B. A. Szost, S. Terzi, F. Martina, D. Boisselier, A. Prytuliak, T. Pirling, M. Hofmann, and D. J. Jarvis, "A comparative study of additive manufacturing techniques: Residual stress and microstructural analysis of CLAD and WAAM printed Ti-6Al-4V components," *Mater. Des.*, vol. 89, pp. 559–567, 2016.

[34] A. A. Antonysamy, J. Meyer, and P. B. Prangnell, "Effect of build geometry on the β -grain structure and texture in additive manufacture of Ti-6Al-4V by selective electron beam melting," vol. 84, pp. 153–168, 2013.

[35] J. Donoghue, J. Sidhu, A. Wescott, and P. Prangnell, "Integration of deformation processing with additive manufacture of Ti-6Al-4V components for improved β grain structure and texture," *TMS Annu. Meet.*, vol. 2015–March, pp. 437–444, 2015.

[36] P. Davies, W. Kockelmann, B. Wynne, R. Eccleston, B. Hutchinson, and W. M. Rainforth, "Validation of neutron texture data on GEM at ISIS using electron backscattered diffraction," *Meas. Sci. Technol.*, vol. 19, pp. 1–4, 2008.

[37] M. Peters and C. Leyens, *Titanium and Titanium Alloys, Fundamentals and Applications*. 2003.

[38] H. E. Coules, L. D. Cozzolino, P. Colegrove, S. Ganguly, S. W. Wen, and T. Pirling, "Neutron Diffraction Analysis of Complete Residual Stress Tensors in Conventional and Rolled Gas Metal Arc Welds," *Exp. Mech.*, vol. 53, pp. 195–204, 2013.

[39] A. M. Stapleton, S. L. Raghunathan, I. Bantounas, H. J. Stone, T. C. Lindley, and D. Dye, "Evolution of lattice strain in Ti-6Al-4V during tensile loading at room temperature," *Acta Mater.*, vol. 56, no. 20, pp. 6186–6196, 2008.

[40] J. Zhang, X. Wang, S. Paddea, and X. Zhang, "Fatigue crack propagation behaviour in wire + arc additive manufactured Ti - 6Al - 4V : Effects of microstructure and residual stress," *Mater. Des. Des.*, vol. 90, pp. 551–561, 2016.

[41] G. Johnson, "Residual Stress Measurement Using Contour Method," The University of Manchester, 2008.

[42] G. Lütjering, "Influence of processing on microstructure and mechanical properties of (α+β) titanium alloys," *Mater. Sci. Eng. A*, vol. 243, pp. 32–45, 1998.

[43]   G. Lutjering and J. C. Williams, "Titanium - 2nd Edition," *Engineering*, p. 442, 2007.

[44]   G. A. Sargent, K. T. Kinsel, A. L. Pilchak, A. A. Salem, and S. L. Semiatin, "Variant Selection During Cooling after Beta Annealing of Ti-6Al-4V Ingot Material," *Metall. Mater. Trans. A*, vol. 43A, pp. 3570–3585, 2012.

[45]   J. W. Elmer, T. A. Palmer, and J. Wong, "In situ observations of phase transitions in Ti-6Al-4V alloy welds using spatially resolved x-ray diffraction," *J. Appl. Phys.*, vol. 93, no. 4, pp. 1941–1947, 2003.

[46]   A. K. Swarnakar, O. Van Der Biest, and B. Baufeld, "Thermal expansion and lattice parameters of shaped metal deposited Ti-6Al-4V," *J. Alloys Compd.*, vol. 509, no. 6, pp. 2723–2728, 2011.

[47]   J. W. Elmer, T. A. Palmer, S. S. Babu, and E. D. Specht, "In situ observations of lattice expansion and transformation rates of ?? and ?? phases in Ti-6Al-4V," *Mater. Sci. Eng. A*, vol. 391, no. 1–2, pp. 104–113, 2005.

[48]   J. W. Elmer, T. A. Palmer, S. S. Babu, and E. D. Specht, "Low temperature relaxation of residual stress in Ti-6Al-4V," *Scr. Mater.*, vol. 52, no. 10, pp. 1051–1056, 2005.

[49]   F. Martina, M. J. Roy, B. A. Szost, S. Terzi, P. A. Colegrove, S. W. Williams, P. J. Withers, J. Meyer, and M. Hofmann, "Residual stress of as-deposited and rolled wire+arc additive manufacturing Ti–6Al–4V components," *Mater. Sci. Technol.*, vol. 836, no. April, 2016.

[50]   J. Ding, P. Colegrove, J. Mehnen, S. Ganguly, P. M. S. Almeida, F. Wang, and S. Williams, "Thermo-mechanical analysis of Wire and Arc Additive Layer Manufacturing process on large multi-layer parts," *Comput. Mater. Sci.*, vol. 50, no. 12, pp. 3315–3322, 2011.

2018-04-08

Residual stress and texture control in þÿTi-6Al-4V wire/+/arc additivel manufactured intersections by stress relief and rolling

Honnige, Jan Roman